

# Quasi-one-dimensional interfacial superconductivity and zero bias peak in a $\text{Bi}_2\text{Te}_3/\text{Fe}_{1+y}\text{Te}$ heterostructure nanowire

Man Kit Cheng <sup>a,b</sup>, Sui Lun Ho <sup>a</sup>, Omargeldi Atanov <sup>a</sup>, Wai Ting Tai <sup>a</sup>, Jing Liang <sup>a,b</sup>, Rolf Lortz <sup>a,\*</sup>, Iam Keong Sou <sup>a,b,\*</sup>

<sup>a</sup>Department of Physics, The Hong Kong University of Science and Technology, Clear Water Bay, Hong Kong, China.

<sup>b</sup>William Mong Institute of Nano Science and Technology, The Hong Kong University of Science and Technology, Hong Kong, China

#Corresponding authors: [phiksou@ust.hk](mailto:phiksou@ust.hk) & [lortz@ust.hk](mailto:lortz@ust.hk)

## Abstract

$\text{Bi}_2\text{Te}_3/\text{Fe}_{1+y}\text{Te}$  heterostructures are known to exhibit interfacial superconductivity between two non-superconducting materials:  $\text{Fe}_{1+y}\text{Te}$  as the parent compound of Fe-based superconducting materials and the topological insulator  $\text{Bi}_2\text{Te}_3$ . Here, we present a top-down approach starting from two-dimensional heterostructures and using a focused ion beam technique to fabricate quasi-one-dimensional  $\text{Bi}_2\text{Te}_3/\text{Fe}_{1+y}\text{Te}$  nanowires. We demonstrate that the  $\text{Bi}_2\text{Te}_3/\text{Fe}_{1+y}\text{Te}$  heterostructure remains intact in narrow nanowire structures with widths on the order of 100 nm and the interfacial superconductivity is preserved, as evidenced by electric transport and Andreev reflection point contact spectroscopy experiments measured at one end of the nanowire. The differential conductance shows a similar superconducting twin-gap structure as in two-dimensional heterostructures, but with enhanced fluctuation effects due to the lower dimensionality. A zero-bias conductance peak indicates either an unconventional nodal order parameter symmetry or the presence of an Andreev bound state, likely related to the inevitable presence of local magnetic moments from the interstitial excess iron in the  $\text{Fe}_{1+y}\text{Te}$  layer, and given the involvement of the

Bi<sub>2</sub>Te<sub>3</sub> topological surface state with a possible link to a Majorana zero mode.

## 1. Introduction

Topological superconductors (SC), especially in the one-dimensional (1D) form, are of great fundamental and technological interest due to their unconventional characteristics. Recent examples of the rich variety of unusual pairing states include the recently predicted and experimentally demonstrated 6-fold nodal Weyl superconducting state in monolayer NbSe<sub>2</sub> [1,2] or the chiral superconducting state, which is thought to be realized in quantum anomalous Hall insulators in proximity contact to a superconductor [3,4]. However, the focus of interest is the potential of topological superconductors to host Majorana modes. In the form of localized Majorana bound states, they promise a topological revolution in quantum computation that is more fault-tolerant [5,6] and exploits their non-Abelian exchange statistics [7,8]. The Majorana bound state or Majorana Zero Mode (MZM) [9] is predicted in various device structures including SC / topological insulators heterostructures [10] and SC/semiconductor heterostructures [11,12]. There are some signature characteristics of MZM such as  $\frac{2e^2}{h}$  quantized conductance [13,14], nonlocal tunnelling [15], and a  $4\pi$ -periodic Josephson effect [16]. In quasi-1D nanostructure devices, a  $\frac{2e^2}{h}$  quantized conductance [17] in the form of a zero-bias conductance peak (ZBCP) in Andreev reflection experiments at the ends of the nanowires and nonlocal tunnelling of electrons (spin-dependent Andreev reflection [18]) are considered as evidence for the existence of MZM, which, however, are often difficult to distinguish from non-topological Andreev-bound states [19]. Numerous devices for MZM searches have been presented, including InSb nanowires in proximity

contact with an NbTiN SC [20], hybrid InSb/Nb nanowire junctions [21-23], Fe atomic chains on Pb [24], HgTe-based topological Josephson junctions [25], proximity-coupled helical hinge states of Bi(111) films decorated with magnetic Fe clusters [26], and two-dimensional (2D) quantum anomalous Hall insulator-superconductor heterostructures [3,4,27]. These devices exhibited some of the characteristic physical properties of MZM, although uncertainties about the origins of the claimed signatures were reported for many of them [19,28-31]. Today, the existence of MZM in none of these systems can be considered proven with certainty, and further research is needed, including new promising systems. It has been proposed that the MZM are localized at the two ends of a nanowire with quasi-1D effective  $p_x+ip_y$ -wave SC, made of a thin-film 2D  $p_x+ip_y$ -wave SC of width  $W$  comparable to or smaller than the superconducting coherence length  $\xi_0$  in a long wire with length  $L \gg \xi_0$  [17]. This can be seen as a transition from the 2D Kane model [32] to the 1D Kitaev model [33] when the width of a long nanowire fabricated from a 2D  $p_x+ip_y$ -wave SC reaches  $\xi_0$ .

Here, we would like to present a promising new approach for the realization of quasi-1D topological SC nanowires fabricated in a relatively simple top-down process using thin-film wafer technology. Recently, we reported that SC occurs at the interface of a  $\text{Bi}_2\text{Te}_3/\text{Fe}_{1+y}\text{Te}$  heterostructure in which both the  $\text{Bi}_2\text{Te}_3$  and  $\text{Fe}_{1+y}\text{Te}$  layers are non-superconducting. The interface of the  $\text{Bi}_2\text{Te}_3/\text{Fe}_{1+y}\text{Te}$  heterostructure exhibits all features of 2D SC with a Berezinski-Kosterlitz-Thouless (BKT) transition [34]. The observation of a robust 2D vortex system [35] and strong anisotropic magnetic responses [36] further confirm the 2D SC character at the interface of  $\text{Bi}_2\text{Te}_3/\text{Fe}_{1+y}\text{Te}$  heterostructure. Most importantly, in a series of point-contact experiments, we uncovered a highly complex superconducting nature with a large pseudogap as well as a superconducting twin-gap structure associated with the superconductivity at the interface and

proximity-induced superconductivity in the  $\text{Bi}_2\text{Te}_3$  layer (which develops at lower temperatures), respectively [37]. In addition, a pronounced zero bias conductance peak (ZBCP) occurred that was robust to high magnetic fields applied perpendicular and parallel to the basal plane. Its origin remains unclear, although the detection of a SC TI material naturally raises hopes that Majorana physics may be at play. The interpretation is complicated, however, as interstitial Fe introduces magnetism into the  $\text{Fe}_{1+y}\text{Te}$  layer [36], and a nodal order parameter symmetry cannot be ruled out as contributing factors or alternative explanations. This encourages further experiments, and we present here an approach to study this heterostructure material in the quasi-1D limit, where a magnetic field applied in parallel to the nanowire is expected to allow such proximity coupled SC nanowires to be tuned into the topological regime [38]. We will describe the fabrication process and the resulting surface morphology and show that the superconducting properties of this heterostructure are preserved in the quasi-1D limit, which includes the multi-gap structure and the ZBCP in the differential conductance of Andreev reflection experiments at the ends of the nanowire.

## **2. Results and Discussion**

### **2.1. Device characterization**

The width of the  $\text{Bi}_2\text{Te}_3/\text{Fe}_{1+y}\text{Te}$  interface of the nanowire cannot be directly deduced from the SEM image because the actual geometry of the fabricated nanowire cannot be represented by a two-dimensional SEM image. Therefore, the width of the  $\text{Bi}_2\text{Te}_3/\text{Fe}_{1+y}\text{Te}$  interface of the nanowire is derived using AFM depth profiling. The corresponding AFM images and data analysis are

provided in Fig. 1. The 3D AFM scan in Fig. 1(a) shows that the surface of the nanowire is flatter than the pristine surface: the surface roughness of the nanowire varies only in a range of a few nanometers. From the height profiles obtained in different regions of Fig. 1(b) (one of the examples is shown in Fig. 1(c) and (d)), the width of the  $\text{Bi}_2\text{Te}_3/\text{Fe}_{1+y}\text{Te}$  interface of the nanowire varies from 80 nm to 120 nm, and the topmost  $10 \text{ nm} \pm 3 \text{ nm}$  were removed during ion milling. However, the shape of the nanowire in the AFM image may be broadened due to the curvature effect of the probe tip (radius of curvature of ScanAsyst-Air probe: 2 - 12 nm) [39]. The width of the  $\text{Bi}_2\text{Te}_3/\text{Fe}_{1+y}\text{Te}$  interface in the nanowire obtained by AFM may thus be overestimated. The AFM results demonstrate that the  $\text{Bi}_2\text{Te}_3$  layer with a thickness of 6 - 9 QL is well connected along the nanowire, so the  $\text{Bi}_2\text{Te}_3/\text{Fe}_{1+y}\text{Te}$  interface should also exist along the entire length of the nanowire.

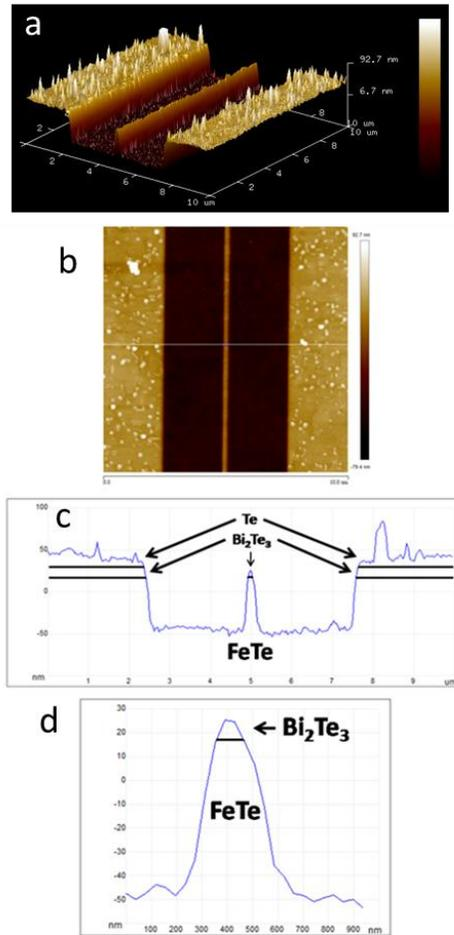


**Figure 1.**  $10\ \mu\text{m} \times 10\ \mu\text{m}$  AFM scans of the  $\text{Bi}_2\text{Te}_3/\text{Fe}_{1+y}\text{Te}$  nanowire: (a) 3D scan; (b) 2D scan and (c) height profile along the white line marked in (b). (d) Enlargement of the height profile of the  $\text{Bi}_2\text{Te}_3/\text{Fe}_{1+y}\text{Te}$  nanowire.

## 2.2. Electrical Resistance

Fig. 2 shows the temperature-dependent electrical resistance below 30 K. The resistance drop begins at 5.5 K and indicates the onset of the superconducting transition. The total resistance is a series combination of the resistance of  $\text{Bi}_2\text{Te}_3/\text{Fe}_{1+y}\text{Te}$  nanowire and the resistance of the regions connecting the nanowire and the bonding pads, in addition to a parallel resistance of the  $\text{Fe}_{1+y}\text{Te}$

layer directly below the nanowire. The latter dominates the temperature-dependent resistance above the superconducting transition but becomes shunned when the interface becomes superconducting [37]. Thus, the residual resistance of 235 Ohm originates from the series contact resistance due to the nature of the two-point probe approach used in this study.

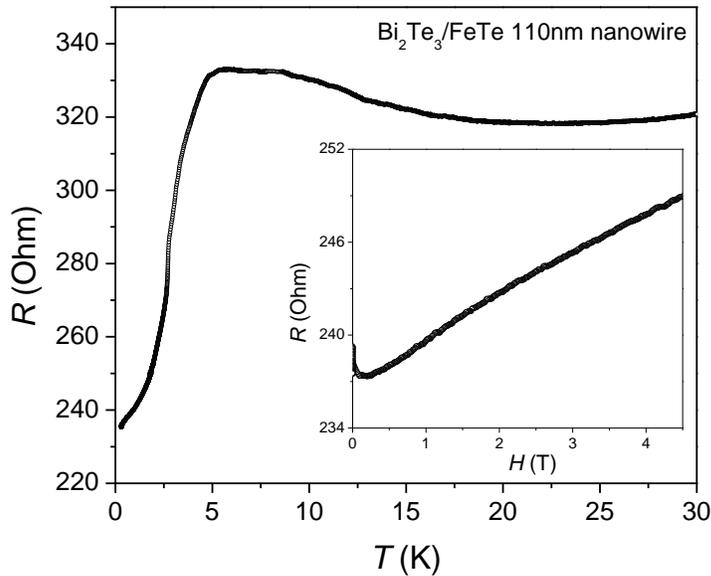


**Figure 2.** Temperature-dependent zero-field resistance in a 110 nm wide  $\text{Bi}_2\text{Te}_3/\text{Fe}_{1+y}\text{Te}$  nanowire device, showing a superconducting transition initiating below 5.5 K. The inset shows magnetoresistance data measured at 300 mK. The direction of the applied magnetic field was parallel to the nanowire. Note that the resistance does not drop to zero due to the series contact resistances in the 2-probe configuration.

The inset in Fig. 2 shows magnetoresistance data measured at 300 mK as a function of descending magnetic field applied parallel to the axis of the nanowire. Apart from a small initial drop in resistance, reversible with increasing or decreasing fields, which could be related either to

the lower critical field or to some magnetic effects related to the interstitial iron excess in the  $\text{Fe}_{1+y}\text{Te}$  layer, it demonstrates that the resistance of the sample increases gradually with the field towards the normal state value, which cannot be reached here because the upper critical field  $H_{c2}$  is much higher at this temperature [34].

### 2.3. Andreev reflection point contact spectroscopy experiments

In Fig. 3a, we show ARPCS data. The differential conductance at 300 mK as a function of bias voltage of the  $\text{Bi}_2\text{Te}_3/\text{Fe}_{1+y}\text{Te}$  nanowire device is shown for different magnetic fields applied parallel to the nanowire, in addition to zero-field data at 4.2 K (slightly below the superconducting onset temperature) and 31.5 K (normal state). The 300 mK spectra show a strong positive Andreev reflection signal extending to very high bias voltages above 40 mV, consistent with our previous data on 2D heterostructures [37], where a very large pseudogap was observed in addition to a superconducting twin gap structure. At 4.2 K, the Andreev contribution is still visible, albeit with much smaller amplitude and significantly broadened, while the normal state data at 31.5 K are completely flat, as expected for a metallic material with ohmic characteristics. An applied magnetic field slightly decreases the overall conductivity at 300 mK, but has little effect on the Andreev contribution, since  $H_{c2}$  is much higher [34]. This is consistent with ARPCS experiments on 2D heterostructures [37], where for parallel or perpendicular fields up to 15 T, only a small effect of the field was found.

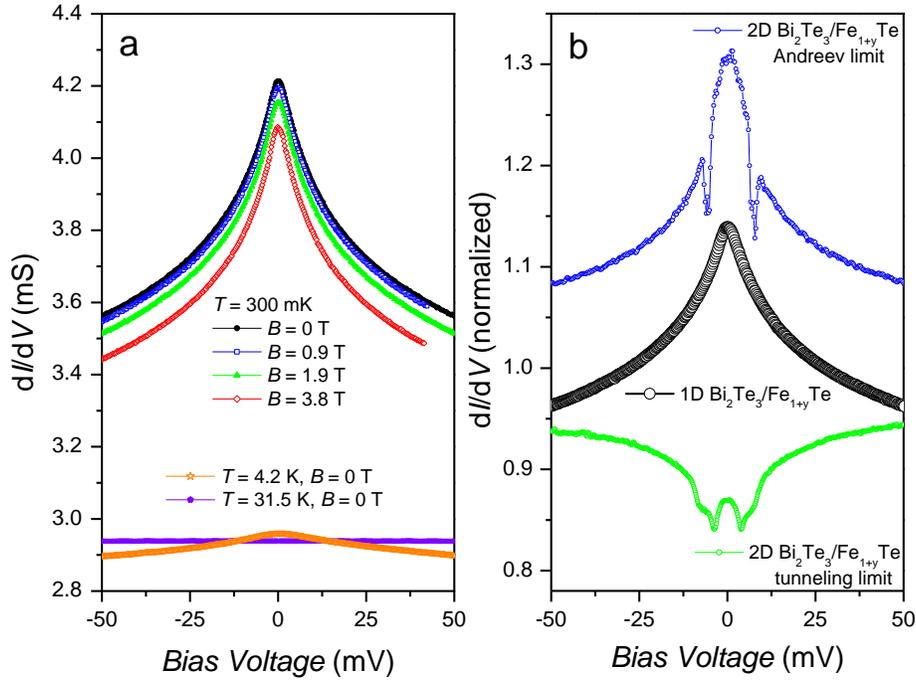


**Figure 3.** a) Point contact Andreev reflection spectroscopy of a 110 nm wide  $\text{Bi}_2\text{Te}_3/\text{Fe}_{1+y}\text{Te}$  nanowire. a) Differential conductance  $dI/dV$  as a function of bias voltage showing a pronounced Andreev reflection signal at 300 mK over a wide bias voltage range, which is hardly influenced by magnetic fields up to 4 T. The Andreev reflection peak is still visible at 4.2 K, while in the normal state at 31.5 K  $dI/dV$  is constant. b) Normalized zero-field  $dI/dV$  data at 300 mK of the 1D  $\text{Bi}_2\text{Te}_3/\text{Fe}_{1+y}\text{Te}$  nanowire (central black data). A comparison with point contact spectroscopy data on 2D  $\text{Bi}_2\text{Te}_3/\text{Fe}_{1+y}\text{Te}$  heterostructures [37] (blue data, high-transparency Andreev limit, green data, low-transparency tunneling limit, scaled up for clarity) shows that the central peak in the 1D nanowire data agrees with the ZBCP observed previously in 2D  $\text{Bi}_2\text{Te}_3/\text{Fe}_{1+y}\text{Te}$  heterostructures.

## 2.4. Discussion

Previously, we reported that 2D  $\text{Bi}_2\text{Te}_3/\text{Fe}_{1+y}\text{Te}$  heterostructures with interfacial superconductivity exhibit a distinct double-gap structure with a zero-bias peak [37], which merge in the low-transparency Andreev limit to form a broad positive peak with some shoulders caused by the gap edges. In Fig. 3b we compare the zero-field data of the  $\text{Bi}_2\text{Te}_3/\text{Fe}_{1+y}\text{Te}$  nanowire recorded at 300 mK with a set of data from such 2D  $\text{Bi}_2\text{Te}_3/\text{Fe}_{1+y}\text{Te}$  heterostructures [37] measured with a needle on the top of the film piercing through both layers (blue data, high-transparency Andreev limit), and with a contact at the edge of the heterostructure (green data, low-transparency tunneling contact). The 1D nanowire data at higher bias voltage are very similar to the data in the Andreev limit of the 2D heterostructure, but at lower bias voltage two shoulder/dip-like structures frame the zero-bias peak in the 2D heterostructure, while data measured in the tunneling limit shows two pairs of shoulder-like structures forming a twin gap with a very similar zero-bias peak inside. No such shoulders or dips can be resolved in the 1D nanowire data, which, as we will show below, is due to reduced quasiparticle lifetime due to enhanced fluctuations in this low dimensionality. However, the comparison shows that the central zero-bias peak, which is even sharper in the 1D nanowires, is consistent with the ZBCP previously observed in 2D  $\text{Bi}_2\text{Te}_3/\text{Fe}_{1+y}\text{Te}$  heterostructures.

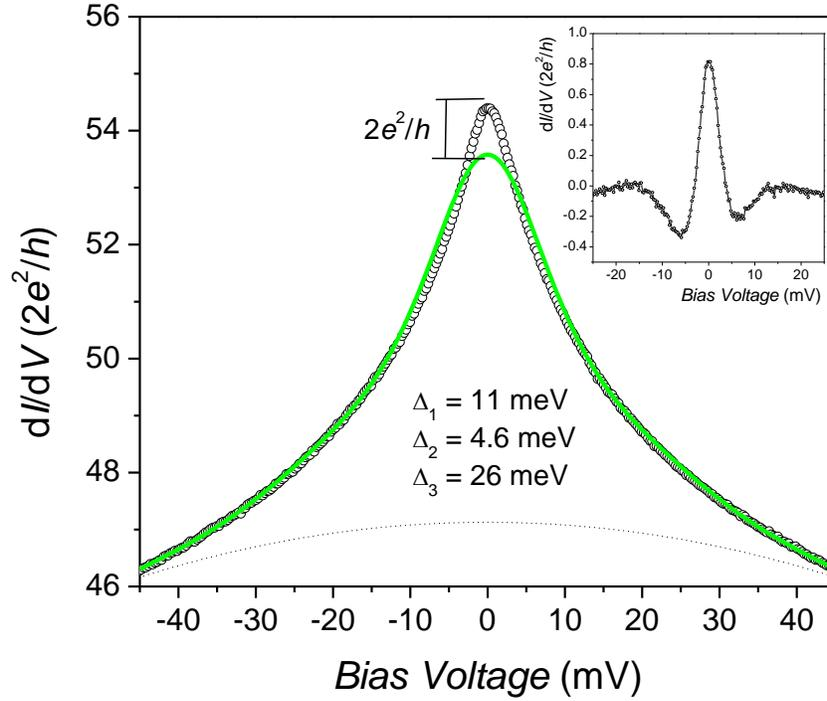


**Figure 4.** Zero-field  $dI/dV$  data at 300 mK of the 1D  $\text{Bi}_2\text{Te}_3/\text{Fe}_{1+y}\text{Te}$  nanowire with a modified Blonder-Tinkham-Klapwijk (BTK) fit (green line) using a three-band model with  $\Delta_1=11$  meV,  $\Delta_2=4.6$  meV and  $\Delta_3=26$  meV (see text for details). In addition, an inverted parabola is used to remove the curved background seen at high bias (dotted line). The zero bias region has been excluded to account for a zero-bias conductance peak. The fitting result suggests that its height is near the quantization value of  $2e^2/h$ . The inset shows the difference between the measured data and the fit, which shows the zero-bias peak and its height clearer.

We analyse the zero-field  $\text{Bi}_2\text{Te}_3/\text{Fe}_{1+y}\text{Te}$  nanowire data by fitting the differential conductance versus bias voltage with a modified 1D Blonder-Tinkham-Klapwijk (BTK) model considering a finite-transparency tunnel junction [40]. Since we are dealing with a low-dimensional superconductor, presumably in the crossover region between the 2D and 1D case, fluctuation effects are expected to be strong, leading to short quasiparticle lifetimes, which we

account for by a large Dynes parameter [41]. To account for the sharp zero-bias peak, we exclude a region on the order of 2-3 meV around zero bias. In addition, we used an inverted parabolic background to account for the curvature in the bias voltage range above 30 mV (dotted line in Fig. 4). The third gap is added to account for the large pseudogap structure previously observed in 2D heterostructures, which extends the Andreev contribution to very high bias voltages [37].

The result of the fit is shown in Fig. 4. The model describes the data very well. The two main superconducting gaps of  $\Delta_1=11$  meV and  $\Delta_2=4.6$  meV are only slightly smaller than the values in 2D heterostructures (12 meV and 6 meV, respectively) [37], which is likely due to the slightly lower  $T_c$  value. With the large Dynes parameters, the structures caused by the 3 gaps merge together to account for the very broad range of the observed Andreev peak of characteristic  $\lambda$  shape, without any shoulder-like structures indicating the edges of the gaps. The ZBCP cannot be accounted for unless an unrealistically small fourth gap were added to the model. In the 2D samples for the low-transparency tunnelling limit, the ZBCP sits as positive peak within the gap depression, while for junctions in the high-transparency Andreev limit it sits on top of the positive Andreev contribution within the gap energy range (Fig 3b). The sharpness of the zero-bias anomaly in our nanowire sample shows that a ZBCP is also present here, even if it merges with the main Andreev peak formed by  $\Delta_1$  and  $\Delta_2$ . Remarkably, the fitting results suggest that the height of the ZBCP is close to the quantization value of  $2e^2/h$ .

To account for the presence of the ZBCP, we also tried to reproduce these data with a two-gap  $d$ -wave model, but no improvement in the fit or significant change in gap values was observed compared to the  $s$ -wave case, although a nodal superconducting order parameter would naturally explain the presence of a ZBCP [42,43].

Our temperature-dependent data indicate that the gaps are quickly smeared and form only a broad bump at 4 K, while well above  $T_c$  at 31.5 K the differential conductance is completely constant, indicating the metallic normal state with ohmic current-voltage characteristics.

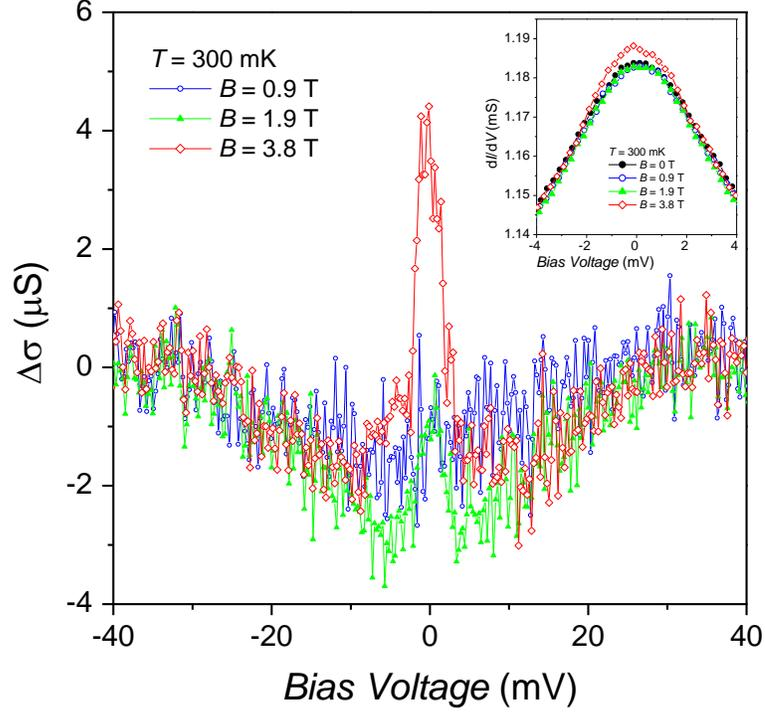


**Figure 5.** Inset: close-up of the zero bias range of differential conductance  $dI/dV$  recorded at 300 mK in different magnetic fields applied parallel to the nanowire axis, showing a slight increase in the zero bias conductance peak height in a field of 4.8 T. Main figure: Difference  $\Delta\sigma$  between the  $dI/dV$  field data and the zero field data showing the increase in the zero-bias conductance peak in the form of a sharp peak .

In our previous report [37], we discussed some possible causes of the ZBCP in 2D heterostructures. It should be noted here that currently neither the superconducting pairing symmetry nor the pairing mechanism of interfacial superconductivity in  $\text{Bi}_2\text{Te}_3/\text{Fe}_{1+y}\text{Te}$  heterostructures is known. Since the parent compound  $\text{Fe}_{1+y}\text{Te}$  of Fe-based superconductors is one

of the building blocks, an unconventional nature of superconductivity is likely. In addition, there is the involvement of the topological surface state of  $\text{Bi}_2\text{Te}_3$  at the interface [34], superconductivity propagating into the topological insulator layer due to the proximity effect [37], and the presence of local magnetism from the interstitial excess iron in the  $\text{Fe}_{1+y}\text{Te}$  layer [36]. A nodal order parameter such as p- or d-wave could naturally account for a ZBCP. The case of unconventional superconductivity on a topological insulator was discussed in Ref. 44. For a topological system, it is expected that for the s-wave case a finite magnetic field is required to induce zero-energy states, while in our samples the ZBCP is already present in zero field. On the other hand, in the case of a  $d_{xy}$ -wave pairing symmetry, for example, a ZBCP is naturally formed in zero field due to resonant states in the middle of the gap. Within a superconducting topological insulator, zero energy states are not spin degenerate, causing a Majorana nature of the fermions in contrast to a topological trivial  $d_{xy}$ -wave superconductor where the zero energy modes are spin degenerate. When a Zeeman field is introduced, the ZBCP may split or becomes suppressed for certain directions.

Our results, including those from Ref. 37, do not indicate any strong field dependence and rule out splitting of the ZBCP. To investigate the effect of a magnetic field on the ZBCP in more detail, we all data recorded in different magnetic fields at 300 mK. If zooming in on the ZBCP in Fig. 5 it can be seen that the ZBCP grows and sharpens slightly in a magnetic field. This is clearer in the inset of Fig. 5 where the zero-field data have been subtracted from the field data: a quite sharp small ZBCP can be seen. This demonstrates that the original height in zero field continues to increase slightly in a parallel field. Unfortunately, due to the short lifespan of our device, it was not possible for us to investigate this in more detail so far.

Another possible explanation for the ZBCP could be related to the excess interstitial iron in  $\text{Fe}_{1+y}\text{Te}$  [42] which could cause Andreev bound states in the gap. It has been shown that odd-

frequency pairing amplitude arises in spatially non-uniform superconductors, attributed here to the excess iron, which can lead to zero-energy Andreev bound states at the the surface or interfaces of the superconductor [45]. The fact that the superconductivity occurs here at the interface with a topological insulator, in addition to the nearly quantized value of the ZBCP, naturally raises the hope that Majorana physics may be involved in such a zero-energy Andreev bound state. On the surface of a topological insulator like  $\text{Bi}_2\text{Te}_3$  there is only one surface Dirac fermion, and in presence of superconducting pairing Majorana modes will appear. When a ferromagnetic insulator is brought into contact with the proximity coupled topological insulator, the emergence of a one-dimensional chiral Majorana mode was predicted as an Andreev bound state, in addition to the MZMs that form in the vortex cores [32,45-47]. Therefore, there are possible scenarios with MZMs that could apply to our case. For 2D  $\text{Bi}_2\text{Te}_3/\text{Fe}_{1+y}\text{Te}$  heterostructures, one would expect localized Majorana zero modes within the vortex cores [32,48]. However, the excess Fe forms strong local magnetic moments with some ferromagnetic exchange at low temperatures, which should lead to spontaneous vortex formation without the need for externally applied magnetic fields [36]. If such a vortex is formed near the point contact, it can cause a ZBCP. Otherwise, clusters of interstitial Fe may directly cause the one-dimensional chiral Majorana mode described above. In a 1D nanowire geometry in proximity to an s-wave superconductor, a field applied parallel to the nanowire axis is expected to drive the material into the topological regime [38], with a pair of localized MZM forming at the opposite ends. Here, the interstitial Fe could provide a local field that allows us to see a ZBCP even without externally applied field. This is supported by the slight increase in the height of the ZBCP in parallel magnetic fields, which aligns the magnetic Fe moments along the nanowire axis. For a detailed understanding of the ZBCP, it is therefore

probably necessary to investigate the role of the interstitial Fe clusters in the  $\text{Fe}_{1+y}\text{Te}$  layer on the superconductivity in more detail.

### 3. Conclusions

We have presented a fabrication process for  $\text{Bi}_2\text{Te}_3/\text{Fe}_{1+y}\text{Te}$  nanowire devices for electrical transport and Andreev reflection point contact spectroscopy experiments at one end of the nanowire. Atomic force microscopy was used to determine the surface morphology of the  $\text{Bi}_2\text{Te}_3/\text{Fe}_{1+y}\text{Te}$  nanowire, demonstrating that the heterostructure remains intact in the nanowire. Electrical transport and Andreev reflection point contact spectroscopy show that the interfacial superconductivity is preserved and exhibits similar characteristics to 2D  $\text{Bi}_2\text{Te}_3/\text{Fe}_{1+y}\text{Te}$  heterostructures with a twin-gap structure and a zero-bias conductance anomaly. While the overall gap structures appear rather smeared due to enhanced fluctuations in the reduced dimensionality, the ZBCP is sharper than in 2D samples and we have discussed possible links to unconventional superconductivity, Andreev bound states from the excess iron in  $\text{Fe}_{1+y}\text{Te}$  or Majorana zero modes. With the present experiment, we are only at the beginning and cannot provide a conclusive explanation for the ZBCP, but these preliminary experiments demonstrate that low-dimensional structures fabricated in a top-down approach from 2D  $\text{Bi}_2\text{Te}_3/\text{Fe}_{1+y}\text{Te}$  heterostructures are a promising approach for further, more detailed experiments to investigate the highly unusual nature of superconductivity in this heterostructure material. Further experiments should ideally be performed on heterostructures with higher  $T_c$  [34] so that lower reduced temperatures  $T/T_c$  are accessible to reduce fluctuations and obtain sharper features. This would be crucial to confirm a quantized value of the ZBCP without the need to rely on a fitting result. Lower transparency

contacts would also be informative to better distinguish the ZBCPs from the superconducting gaps, as well as microscopic experiments, e.g. with a scanning tunneling probe, to see if there is a connection between the ZBCP and the excess iron.

## 4. Experimental Section

*Device fabrication:* The  $\text{Bi}_2\text{Te}_3/\text{Fe}_{1+y}\text{Te}$  nanowire device was fabricated from a  $\text{Bi}_2\text{Te}_3/\text{Fe}_{1+y}\text{Te}$  thin film heterostructure sample grown in a VG V80H MBE system. The structure of the  $\text{Bi}_2\text{Te}_3/\text{Fe}_{1+y}\text{Te}$  thin film sample is Te (10nm)/ $\text{Bi}_2\text{Te}_3$  (8-9nm)/ $\text{Fe}_{1+y}\text{Te}$  (220nm)/ZnSe (80nm)/ $n^+$  GaAs (001). The ZnSe layer serves as buffer layer and Te as a capping layer for protection. The thin film sample was cut into a small piece with an area of  $2\text{mm} \times 4\text{mm}$  and transferred into an FEI Helios G4 UX dual-beam Focused Ion Beam (FIB) / Field Emission Scanning Electron Microscope (FESEM) system for ion milling and Pt electrode deposition was applied to fabricate the  $\text{Bi}_2\text{Te}_3/\text{Fe}_{1+y}\text{Te}$  nanowire and the corresponding device for electrical transport measurements. Scanning Electron Microscope (SEM) images were acquired using the dual-beam FIB/FESEM system. Surface morphology with depth profile of the  $\text{Bi}_2\text{Te}_3/\text{Fe}_{1+y}\text{Te}$  nanowire was obtained using a Bruker Dimension ICON Atomic Force Microscope (AFM) with a ScanAsyst-Air probe, and the results were analyzed by NanoScope Analysis software. Ti(5nm)/Au(70nm) bonding pads were deposited onto the device using a Denton Vacuum Desk Top Pro desktop sputtering system. Electrical contacts were made with Al wires bonded by an ASM AB520 wedge bonder. High Resolution Transmission Electron Microscopy (HRTEM) images were captured using a JEOL JEM 2010F TEM.

Fig. 6 shows a schematic diagram of the fabrication process of  $\text{Bi}_2\text{Te}_3/\text{Fe}_{1+y}\text{Te}$  nanowires

for electrical measurements with two probes. The thicknesses of the different layers of the thin film sample were measured using the HRTEM images shown in Fig. 7. The  $\text{Bi}_2\text{Te}_3/\text{Fe}_{1+y}\text{Te}$  nanowires were fabricated in the dual-beam FIB/FESEM system using a  $\text{Ga}^+$  ion beam source at 30 keV. The ion beam source current ranged from 1 pA to 65 nA for different aspects. A high surface flatness region was used to fabricate the  $\text{Bi}_2\text{Te}_3/\text{Fe}_{1+y}\text{Te}$  nanowire, which was investigated using tilted SEM and FIB images. The FIB source current for image acquisition was set to 1 pA to reduce damage to the sample. Optimized currents were selected for ion milling at different scales. Then, a 30  $\mu\text{m}$  long  $\text{Bi}_2\text{Te}_3/\text{Fe}_{1+y}\text{Te}$  nanowire was fabricated by ion milling and the nearby  $\text{Bi}_2\text{Te}_3$  layer was removed to ensure that the SC properties were dominated by the  $\text{Bi}_2\text{Te}_3/\text{Fe}_{1+y}\text{Te}$  nanowire in transport and differential conductivity measurements. The unetched part near the  $\text{Bi}_2\text{Te}_3/\text{Fe}_{1+y}\text{Te}$  nanowire is used for height calibration.

The  $\text{Bi}_2\text{Te}_3$  layer near the expected position of the Pt and Ti/Au electrodes was also removed for the reasons mentioned above. The FeTe and ZnSe layers with a width of 5  $\mu\text{m}$  on the two sides near the center of the nanowire were removed up to the two top/bottom edges of the device (Fig. 6) to prevent a short circuit. After the ion milling, Pt wires with a cross-sectional area of  $300 \times 300$  nm were deposited to connect the two ends of the nanowire to the positions of the Ti/Au bonding pads. Then the device was transferred to the sputtering system and the two ends of the device were coated with Ti/Au electrodes. Finally, the device was mounted on a ceramic leadless chip carrier (CLCC) with paraffin wax, and the two Ti/Au bonding pads were connected with the pads on the CLCC by Al bonding wires. Fig. 8(a) and (b) show SEM images of the  $\text{Bi}_2\text{Te}_3/\text{Fe}_{1+y}\text{Te}$  nanowire.

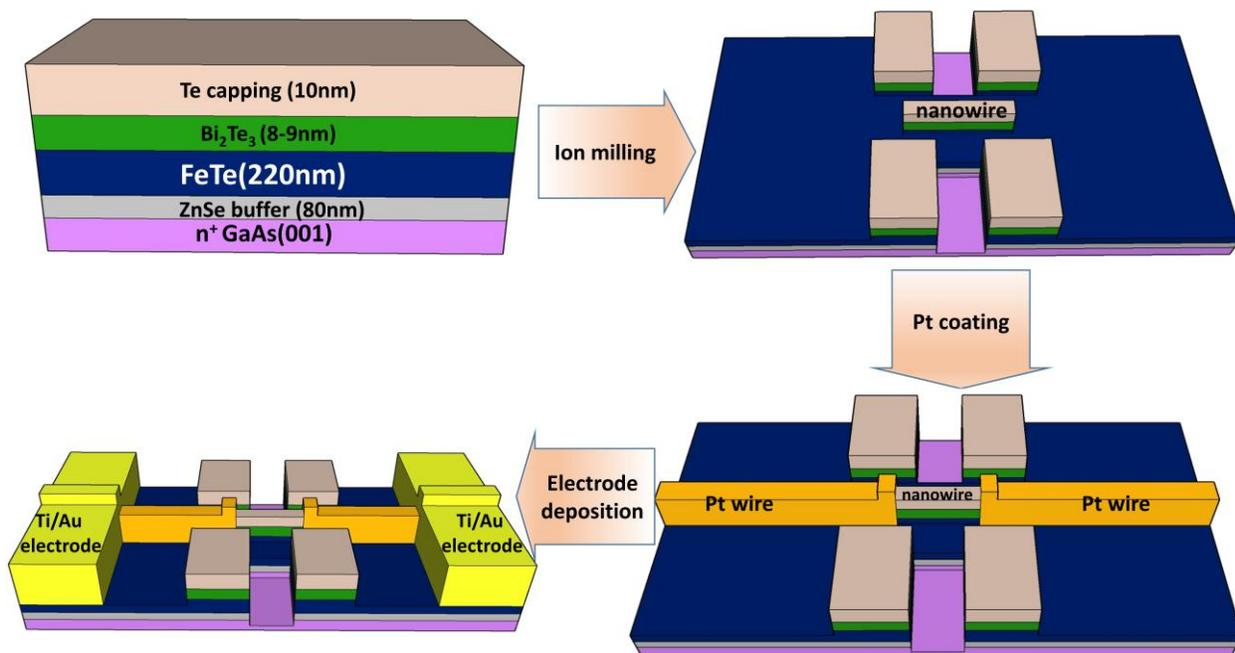


**Figure 6.** Schematic drawings of the fabrication processes of the  $\text{Bi}_2\text{Te}_3/\text{Fe}_{1+y}\text{Te}$  nanowire device for two-point probe electrical transport and Andreev reflection point contact measurements.

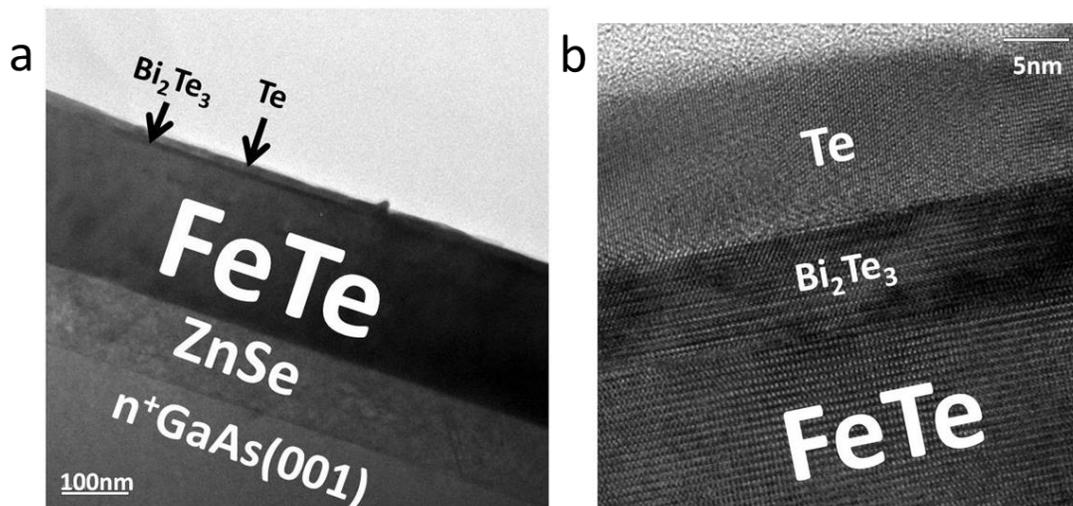


**Figure 7.** The cross-sectional HRTEM image of the  $\text{Bi}_2\text{Te}_3/\text{Fe}_{1+y}\text{Te}$  thin film sample. (a) The full picture of the sample; (b) close-up image near the  $\text{Bi}_2\text{Te}_3/\text{Fe}_{1+y}\text{Te}$  interface.

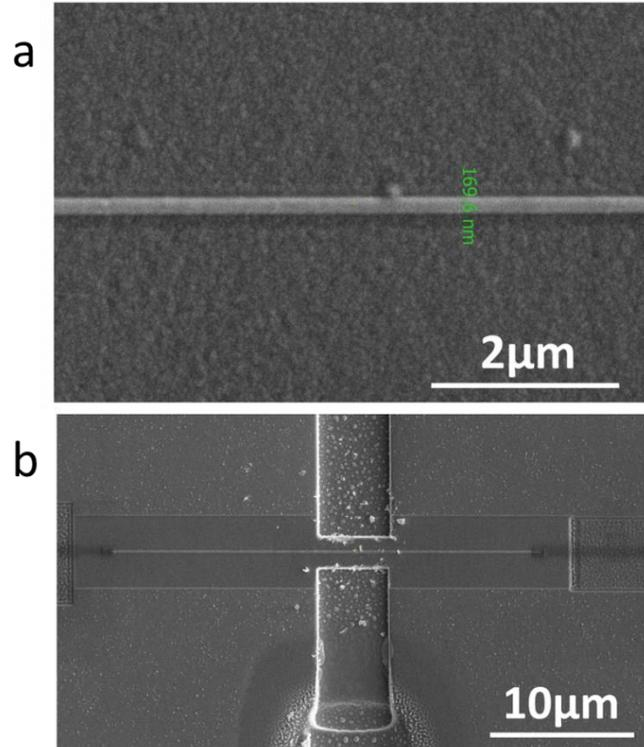


**Figure 8.** The SEM images of (a) the close-up and (b) full picture of  $\text{Bi}_2\text{Te}_3/\text{Fe}_{1+y}\text{Te}$  nanowire.

*Electrical transport and point contact Andreev reflection experiments:* Electrical transport and Andreev reflection point contact spectroscopy (ARPCS) measurements were conducted using a Keithley 6221 AC/DC current source, a 34411A digital multimeter, and an SR830 lock-in amplifier. The electrical transport experiments were performed in AC mode at a frequency on the order of 10 Hz in combination with the lock-in-amplifier. For the point contact spectroscopy, the current source generated an AC current with variable DC offset. The DC component induces the bias voltage by injecting the current in small steps from a negative value to a positive value across the point contact formed by the Pt electrode at one end of the nanowire, while the other side was grounded. The DC bias voltage was measured using the digital multimeter. The AC current with a constant amplitude comparable to the step size of the bias current scan was used to determine the

differential conductance  $dI/dV$  as a function of the measured bias voltage.

## **Acknowledgements**

M.K.C. and S.L.H. contributed equally to this work. We thank U. Lampe for technical assistance with the low-temperature experiments. The authors acknowledge funding by the Research Grants Council of the Hong Kong Special Administrative Region, China, under Grant Numbers 16308020, 16302018, 16302319, C6025-19G, SBI17SC14 and IEG16SC03.

## **Conflict of Interest**

The authors declare no conflict of interest.

## **Data Availability Statement**

The data that support the findings of this study are available from the corresponding author upon reasonable request.

## **Keywords**

topological superconductivity, interfacial superconductivity, quasi-one-dimensional superconductivity, Andreev reflection point contact spectroscopy, Majorana zero mode

- [1] W.-Y. He, B. T. Zhou, J. J. He, N. F. Q. Yuan, T. Zhang, K. T. Law, Magnetic field driven nodal topological superconductivity in monolayer transition metal dichalcogenides. *Commun. Phys.* **2018**, *1*, 40.
- [2] C.-w. Cho, J. Lyu, L. An, T. Han, K. T. Lo, C. Y. Ng, J. Hu, Y. Gao, G. Li, M. Huang, N. Wang, J. Schmalian, R. Lortz, Nodal and nematic superconducting phases in NbSe<sub>2</sub> monolayers from competing superconducting channels, *Phys. Rev. Lett.* **2022**, *in press*, arXiv:2003.12467.
- [3] Z.-L. Qi, T. L. Hughes, S. C. Zhang, Chiral topological superconductor from the quantum Hall state, *Phys. Rev. B* **2010**, *82*, 184516.
- [4] J. Shen, J. Lyu, J. Z. Gao, Y.-M. Xie, C.-Z. Chen, C.-w. Cho, O. Atanov, Z. Chen, K. Liu, Y. J. Hu, K. Yau Yip, S. K. Goh, Q. L. He, L. Pan, K. L. Wang, K. T. Law, R. Lortz, Spectroscopic fingerprint of chiral Majorana modes at the edge of a quantum anomalous Hall insulator/superconductor heterostructure, *Proc. Natl. Acad. Sci. U.S.A.* **2019**, *117*, 238-242.
- [5] C. Nayak, S. H. Simon, A. Stern, M. Freedman, S. Das Sarma, Non-Abelian anyons and topological quantum computation, *Rev. Mod. Phys.* **2008**, *80*, 1083–1159.
- [6] N. R. Ayukaryana, M. H. Fauzi, E. H. Hasdeo, The Quest and hope of majorana zero modes in topological superconductor for fault-tolerant quantum computing: An introductory overview. *AIP Conf. Proc.* **2021**, *2382*, 020007.
- [7] T. Hyart, B. van Heck, I. C. Fulga, M. Burrello, A. R. Akhmerov, C. W. Beenakker, Flux-controlled quantum computation with Majorana fermions, *Phys. Rev. B* **2013**, *88*, 035121.

- [8] B. Lian, X.-Q. Sun, A. Vaezi, X.-L. Qi, S.-C. Zhang, Topological quantum computation based on chiral Majorana fermions, *Proc. Natl. Acad. Sci. U.S.A.* **2018**, *115*, 10938–10942.
- [9] F. Wilczek, Majorana returns, *Nat. Phys.* **2009**, *5*, 614–618.
- [10] J. C. Teo, C. L. Kane, Topological defects and gapless modes in insulators and superconductors, *Phys. Rev. B* **2010**, *82*, 115120.
- [11] R. M. Lutchyn, J. D. Sau, S. Das Sarma, Majorana fermions and a topological phase transition in semiconductor-superconductor heterostructures, *Phys. Rev. Lett.* **2010**, *105*, 077001.
- [12] Y. Oreg, G. Refael, F. von Oppen, Helical liquids and Majorana bound states in quantum wires, *Phys. Rev. Lett.* **2010**, *105*, 177002.
- [13] K. T. Law, P. A. Lee, T. K. Ng, Majorana fermion induced resonant Andreev reflection, *Phys. Rev. Lett.* **2009**, *103*, 237001.
- [14] M. Wimmer, A. R. Akhmerov, J. P. Dahlhaus, C. W. Beenakker, Quantum Point contact as a probe of a topological superconductor, *New J. Phys.* **2011**, *13*, 053016.
- [15] J. Nilsson, A. R. Akhmerov, C. W. Beenakker, Splitting of a Cooper pair by a pair of Majorana bound states, *Phys. Rev. Lett.* **2008**, *101*, 20403.
- [16] H. J. Kwon, K. Sengupta, V. M. Yakovenko, Theoretical prediction of the fractional ac Josephson effect in p- and d-wave superconductors, *Braz. J. Phys.* **2003**, *33*, 653–658.
- [17] A. C. Potter, P. A. Lee, Multichannel generalization of Kitaev's majorana end states and a practical route to realize them in thin films, *Phys. Rev. Lett.* **2010**, *105*, 227003.
- [18] T. Mizushima, Non-local manipulation of local tunneling processes through Majorana zero modes, *JPSJ News Comments* **2017**, *14*, 14.

- [19] C.-X. Liu, J. D. Sau, T. D. Stanescu, S. Das Sarma, Andreev bound states versus Majorana bound states in quantum dot-nanowire-superconductor hybrid structures: Trivial versus topological zero-bias conductance peaks, *Phys. Rev. B* **2017**, *96*, 075161.
- [20] V. Mourik, K. Zuo, S. M. Frolov, S. R. Plissard, E. P. Bakkers, L. P. Kouwenhoven, Signatures of Majorana fermions in hybrid superconductor-semiconductor nanowire devices, *Science* **2012**, *336*, 1003–1007.
- [21] L. P. Rokhinson, X. Liu, J. K. Furdyna, The fractional A.C. Josephson effect in a semiconductor–superconductor nanowire as a signature of Majorana particles, *Nat. Phys.* **2012**, *8*, 795–799.
- [22] H. O. Churchill, V. Fatemi, K. Grove-Rasmussen, M. T. Deng, P. Caroff, H. Q. Xu, C. M. Marcus, Superconductor-nanowire devices from tunneling to the multichannel regime: Zero-bias oscillations and magnetoconductance crossover, *Phys. Rev. B* **2013**, *87*, 241401.
- [23] M. T. Deng, C. L. Yu, G. Y. Huang, M. Larsson, P. Caroff, H. Q. Xu, Anomalous zero-bias conductance peak in a Nb-InSb nanowire–Nb hybrid device, *Nano Lett.* **2012**, *12*, 6414–6419.
- [24] S. Nadj-Perge, I. K. Drozdov, J. Li, H. Chen, S. Jeon, J. Seo, A. H. MacDonald, B. A. Bernevig, A. Yazdani, Observation of Majorana fermions in ferromagnetic atomic chains on a superconductor, *Science* **2014**, *346*, 602–607.
- [25] J. Wiedenmann, E. Bocquillon, R. S. Deacon, S. Hartinger, O. Herrmann, T. M. Klapwijk, L. Maier, C. Ames, C. Brüne, C. Gould, A. Oiwa, K. Ishibashi, S. Tarucha, H. Buhmann, L. W. Molenkamp,  $4\pi$ -periodic Josephson supercurrent in HgTe-based topological Josephson junctions, *Nat. Commun.* **2016**, *7*, 10303.

- [26] B. Jäck, Y. Xie, Jian Li, S. Jeon, B. A. Bernevig, A. Yazdani, Observation of a Majorana zero mode in a topologically protected edge channel, *Science* **2019**, *364*, 1255–1259.
- [27] Q. L. He, L. Pan, A. L. Stern, E. C. Burks, X. Che, G. Yin, J. Wang, B. Lian, Q. Zhou, E. S. Choi, K. Murata, X. Kou, Z. Chen, T. Nie, Q. Shao, Y. Fan, S.-C. Zhang, K. Liu, J. Xia, K. L. Wang, Chiral Majorana fermion modes in a quantum anomalous hall insulator–superconductor structure, *Science* **2017**, *357*, 294–299.
- [28] M. Kayyalha, D. Xiao, R. Zhang, J. Shin, J. Jiang, F. Wang, Y.-F. Zhao, R. Xiao, L. Zhang, K. M. Fijalkowski, P. Mandal, M. Winnerlein, C. Gould, Q. Li, L. W. Molenkamp, M. H. Chan, N. Samarth, C.-Z. Chang, Absence of evidence for chiral Majorana modes in quantum anomalous Hall-superconductor devices, *Science* **2020**, *367*, 64–67.
- [29] P. Yu, J. Chen, M. Gomanko, G. Badawy, E. P. Bakkers, K. Zuo, V. Mourik, S. M. Frolov, Non-Majorana states yield nearly quantized conductance in proximatized nanowires, *Nat. Phys.* **2021**, *17*, 482–488.
- [30] S. Frolov, Quantum Computing’s reproducibility crisis: Majorana fermions, *Nature* **2021**, *592*, 350–352.
- [31] M. C. Dartiailh, J. J. Cuzzo, B. H. Elfeky, W. Mayer, J. Yuan, K. S. Wickramasinghe, E. Rossi, J. Shabani, Missing Shapiro steps in topologically trivial Josephson junction on InAs Quantum well, *Nat. Commun.* **2021**, *12*, 78.
- [32] L. Fu, C. L. Kane, Superconducting proximity effect and Majorana fermions at the surface of a topological insulator, *Phys. Rev. Lett.* **2008**, *100*, 096407.
- [33] A. Y. Kitaev, Unpaired Majorana fermions in quantum wires, *Phys.-Uspekhi* **2001**, *44*, 131.

- [34] Q. L. He, H. Liu, M. He, Y. H. Lai, H. He, G. Wang, K. T. Law, R. Lortz, J. Wang, I. K. Sou, Two-dimensional superconductivity at the interface of a  $\text{Bi}_2\text{Te}_3/\text{FeTe}$  heterostructure, *Nat. Commun.* **2014**, *5*, 4247.
- [35] H.-C. Liu, H. Li, Q. L. He, I. K. Sou, S. K. Goh, J. Wang, Robust two-dimensional superconductivity and Vortex System in  $\text{Bi}_2\text{Te}_3/\text{FeTe}$  heterostructures, *Sci. Rep.* **2016**, *6*, 26168.
- [36] Q. L. He, M. He, J. Shen, Y. H. Lai, Y. Liu, H. Liu, H. He, G. Wang, J. Wang, R. Lortz, I. K. Sou, Anisotropic magnetic responses of a 2D-superconducting  $\text{Bi}_2\text{Te}_3/\text{FeTe}$  heterostructure, *J. Phys.: Cond. Mat.* **2015**, *27*, 345701.
- [37] M. Q. He, J. Y. Shen, A. P. Petrović, Q. L. He, H. C. Liu, Y. Zheng, C. H. Wong, Q. H. Chen, J. N. Wang, K. T. Law, I. K. Sou, R. Lortz, Pseudogap and proximity effect in the  $\text{Bi}_2\text{Te}_3/\text{Fe}_{1+y}\text{Te}$  interfacial superconductor, *Sci. Rep.* **2016**, *6*, 32508.
- [38] A. Cook and M. Franz. Majorana fermions in a topological-insulator nanowire proximity-coupled to an s-wave superconductor. *Phys. Rev. B* **2011**, *84*, 201105.
- [39] C. Canale, B. Torre, D. Ricci, P. C. Braga, Recognizing and avoiding artifacts in atomic force microscopy imaging, *Methods in Molecular Biology* (2011) pp. 31–43.
- [40] G. E. Blonder, M. Tinkham, T. M. Klapwijk, Transition from metallic to tunneling regimes in superconducting microconstrictions: excess current, charge imbalance, and supercurrent conversion. *Phys. Rev. B* **1982**, *25*, 4515.
- [41] C. Dynes, V. Naraynamurti, J. P. Garno, Direct measurement of quasiparticle-lifetime broadening in a strong-coupled superconductor. *Phys. Rev. Lett.* **1978**, *41*, 1509.
- [42] Y. Tanaka, S. Kashiwaya, Theory of Tunneling Spectroscopy of d-Wave Superconductors, *Phys. Rev. Lett.* **1995**, *74*, 3451.

- [43] S. Kashiwaya, Y. Tanaka, Tunnelling effects on surface bound states in unconventional superconductors, *Rep. Prog. Phys.* **2000**, *63*, 1641–1724.
- [44] J. Linder, Y. Tanaka, T. Yokoyama, A. Sudbø, N. Nagaosa, Unconventional Superconductivity on a Topological Insulator, *Phys Rev Lett.* **2010**, *104*, 067001.
- [45] Y. Tanaka, M. Sato, N. Nagaosa, Symmetry and Topology in Superconductors —Odd-Frequency Pairing and Edge States—*J. Phys. Soc. Jap.* **2012**, *81*, 011013.
- [46] M. Z. Hasan, C. L. Kane, Colloquium: Topological insulators, *Rev. Mod. Phys.* **2010**, *82*, 3045.
- [47] X.-L. Qi, S.-C. Zhang, Topological insulators and superconductors, *Rev. Mod. Phys.* **2011**, *83*, 1057.
- [48] J.-X. Yin, Z. Wu, J.-H. Wang, Z.-Y. Ye, J. Gong, X.-Y. Hou, L. Shan, A. Li, X.-J. Liang, X.-X. Wu, J. Li, C.-S. Ting, Z.-Q. Wang, J.-P. Hu, P.-H. Hor, H. Ding, S. H. Pan, Observation of a robust zero-energy bound state in iron-based superconductor Fe(Te,Se), *Nat. Phys.* **2015**, *11*, 543–546.